The Role of Fault Rock Fabric in the Dynamics of Laboratory Faults

Giacomo Pozzi[1] , **Marco M. Scuderi[2]** , **Elisa Tinti[1,2]** , **Manuela Nazzari[1], and Cristiano Collettini[1,2]**

[1]Istituto Nazionale Di Geofisica e Vulcanologia (INGV), Rome, Italy, [2]Dipartimento di Scienze della Terra, La Sapienza Università di Roma, Rome, Italy

Abstract Fault stability is inherently linked to the frictional and healing properties of fault rocks and associated fabrics. Their complex interaction controls how the stored elastic energy is dissipated, that is, through creep or seismic motion. In this work, we focus on the relevance of fault fabrics in controlling the reactivation and slip behavior of dolomite-anhydrite analog faults. We designed a set of laboratory experiments where we first develop fault rocks characterized by different grain size reduction and localization at normal stresses of σ_N = 15, 35, 60, and 100 MPa and second, we reload and reactivate these fault rocks at the frictional stability transition, achieved at σ_N = 35 MPa by reducing the machine stiffness. If normal stress is lowered this way, reactivation occurs with relatively large stress drops and large peak-slip velocities. Subsequent unstable behavior produces slow stick-slip events with low stress drop and with either asymmetric or Gaussian slip velocity function depending on the inherited fault fabric. If normal stress is raised, deformation is accommodated within angular cataclasites promoting stable slip. The integration of microstructural data (showing brittle reworking of preexisting textures) with mechanical data (documenting restrengthening and dilation upon reactivation) suggests that frictional and chemically assisted healing, which is common in natural faults during the interseismic phase, can be a relevant process in developing large instabilities. We also conclude that fault rock heterogeneity (fault fabric) modulates the slip velocity function and thus the dynamics of repeating stick-slip cycles.

Plain Language Summary Displacement is accommodated within the Earth's upper crust through motion along fault zones. These fault zones are composed of a wide variety of deformed rocks, which are characterized by different geometric (e.g., inner textures) and physico-chemical properties. Such complexity is key in controlling how the elastic energy stored in the loading medium surrounding the fault will be dissipated in time, for example, through slow (aseismic creep) or fast slip (earthquakes). This study presents a series of laboratory experiments where: (a) a range of pressures are applied to form fault rocks characterized by different inner textures; and then (b) the fault rocks are reactivated at the same experimental conditions, chosen to favor unstable sliding as documented in previous experiments in the same material. The observed slip behavior of reactivated faults indicates that the fault's inner textures greatly influence how our experimental faults move. For instance, fault motion is observed to occur constantly in presence of heterogeneous slip zones, and rhythmically (a behavior known as stick-slip) in homogenous, fine-grained slip zones. Chemically assisted processes, favored by high pressures and the presence of fluids, promote rehealing of the fault, favoring reactivation with energetic slip events that can be as fast as earthquakes.

1. Introduction

The relationship between fault rock structure and associated fault slip behavior represents a crucial point in fault mechanics and structural geology (e.g., Fagereng & Beall, 2021; Sibson, 1977). Rock deformation experiments and seismological studies have been developed and often integrated to improve our understanding on this topic (e.g., McLaskey et al., 2014; Nielsen et al., 2016; Passelègue et al., 2016; Vidale et al., 1994). In 1966, Brace and Byerlee (1966) presented experimental evidence for Reid's theory of the elastic rebound and proposed the stick-slip behavior, observed during frictional sliding of Westerly granite, as the primary mechanism in earthquake physics. Since then, numerous laboratory experiments have been developed to capture different aspects of earthquake physics.

Since the formulation of the rate and state frictional framework, a large number of experimental studies have sought the link between the frictional constitutive parameters, frictional stability, and the fault zone structure (e.g., Beeler et al., 1996; Dieterich, 1979; Marone, 1998). It has been discovered that fault frictional stability is influenced by slip localization (Beeler et al., 1996; Marone, 1998), mineralogy (e.g., Collettini et al., 2019; Ikari, Marone, & Saffer, 2011), grain properties (e.g., Mair et al., 2002), fault roughness (e.g., Goebel et al., 2017; Harbord et al., 2017), chemical processes (e.g., Niemeijer & Spiers, 2007), and initial effective normal stress (Passelègue et al., 2020). Nonetheless, a recent conundrum in fault mechanics is represented by the discovery of slow slip events (e.g., Bürgmann, 2018; Kirkpatrick et al., 2021), and associated quasi-dynamic transients (Peng & Gomberg, 2010). In this context, there are still many open questions that need to be addressed such as what is the mechanics that keeps the slip velocity slow during propagation. Understanding the coupling between typical fault rocks observed in the environments where slow slips are documented and their frictional behaviors is paramount to find an answer (e.g., Bürgmann, 2018; Fagereng et al., 2014; Kirkpatrick et al., 2021; Nie & Barbot, 2021).

The spectrum of slip behavior of natural faults, ranging from creep to slow and fast earthquakes, has been successfully reproduced in laboratory experiments by changing the effective normal stress, the frictional properties of the experimental fault, and the loading stiffness (Bedford & Faulkner, 2021; Leeman et al., 2016; Mclaskey & Yamashita, 2017; Passelègue et al., 2019; Scuderi et al., 2016; Shreedharan et al., 2020). The details of stick-slip dynamics have been recently documented with shear experiments. Slip velocity functions with Gaussian shapes have been observed in fine-grained materials (Tinti et al., 2016) or bare rock-surfaces (Mclaskey & Yamashita, 2017), whereas asymmetric velocity functions have been observed in heterogeneous fault rocks (Scuderi et al., 2020). Whether slip velocities represent an average value of the whole fault or a local feature of an extended fault, these observations have raised questions on whether the kinematic rupture history and shear stress evolution during an unstable event can be associated to the resulting fault rocks.

Together with laboratory experiments, ancient faults exposed at the surface have been used to infer the deformation processes at play within the seismogenic layer (e.g., Chester et al., 1993; Rowe & Griffith, 2015; Sibson, 1977). These studies show that faults are made of a variety of clastic rocks (cataclasites; Sibson, 1977) which are built by reworking of the original materials during fault slip. Most of these rocks are cohesive, which means that the cataclastic material is chemically bound and presents resistance to deformation comparable to that of an intact rock. This is the result of both frictional and chemical healing promoted by pressure-solution, crack-sealing, plastic deformation at grain contacts, porosity reduction, and the precipitation of new mineral phases (Bos et al., 2000; Chester et al., 1993; Cox, 2017; Renard et al., 2000; Sibson, 1992; Tarling et al., 2018). Laboratory experiments show that fault healing and associated strength recovery can be achieved through both fluid-assisted cementation of fault gouge (e.g., Bos et al., 2000; Muhuri et al., 2003; Tenthorey et al., 2003; Yasuhara et al., 2005), via frictional healing following plastic deformation at grain contacts (e.g., Dieterich & Kilgore, 1994; Karner & Marone, 1998; Renard et al., 2012) and welding by frictional melt immediately after the propagation of an earthquake (Hayward & Cox, 2017; Mitchell et al., 2016). Such processes are extremely relevant during the post- and inter-seismic period, when the faults are mainly locked or slowly creeping, and may act to develop the cohesive fault rocks that are abundant within the seismogenic layer (Sibson, 1977). Some experimental evidence shows that reactivation (RA) of cemented faults promotes unstable failure with large stress drops (Carpenter et al., 2014), the transition from stable to potentially unstable slip (Ikari & Hüpers, 2021), and a nearly instantaneous weakening phase (Smith et al., 2015). Furthermore, microphysical models based on pressure solution and fault fabric have been proven successful in reproducing a spectrum of slip behaviors (Chen & Spiers, 2016; van den Ende et al., 2018).

From this description, it emerges the need to improve our understanding on the causal relation between the mechanics (i.e., frictional evolution) and the fault rock structure. In this work, we integrate mechanical data with detailed microstructural studies to show how inherited fault rock fabrics radically change the slip behavior and shear stress evolution upon RA, even when all of the experimental conditions and materials are kept the same.

2. Methods

Simulated fault gouges (fine-grained rock powders) were tested using the bi-triaxial apparatus BRAVA (Figure 1a, Collettini et al., 2014) in a double-direct shear configuration (DDS hereinafter, Figure 1b). Experiments were performed at room pressure and temperature conditions, and 100% relative humidity. The DDS consists of two
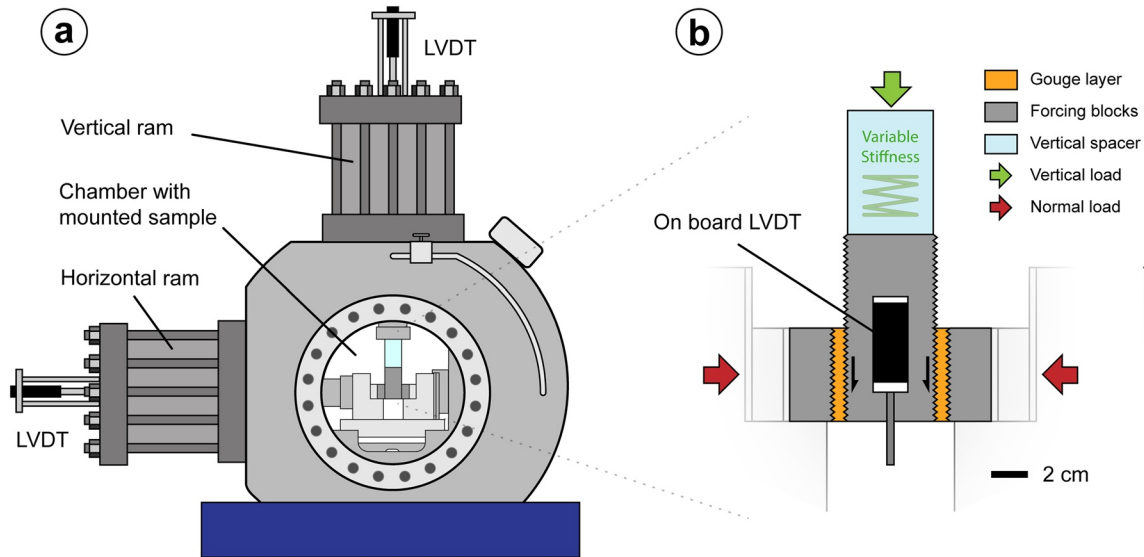
Figure 1. (a) Sketch of the bi-triaxial apparatus BRAVA with the sample fully mounted in the open chamber. (b) Enlarged sketch of the ensembled double direct shear (DDS) configuration for rock powders.

3 mm thick gouge layers sandwiched between a central (slider) and two lateral (stationary) forcing blocks as shown in Figure 1b. All forcing blocks are grooved to ensure deformation localisation within the simulated gouge layer. A high-precision ($\pm$0.1 µm), linear variable differential transformer (LVDT) is mounted on the central slider, providing an accurate measurement of the simulated fault motion, and avoiding potential artifacts due to the elasticity of the machine. Further details on methods and postprocessing of data are included in Supporting Information S1, information about the synchronization of the data set acquired with BRAVA is presented in Tinti et al. (2016). The chosen powders are a mixture of pure anhydrite and dolomite (50%–50% vol.), crushed and sieved to obtain a grain size <63 µm. The mixture is used as a proxy of fault gouge of the Triassic evaporites of the Apennines (Scuderi et al., 2013), a layer hosting relevant seismic activity (De Paola et al., 2008). To ensure full penetration of water within the gouge layer we left the layers overnight within a 100% humidity chamber before sample assembly.

Friction experiments consisted of two fundamental stages: (a) texturing (TX) and (b) RA. During TX stage samples are deformed at constant normal stress of σ_N = 15, 35, 60, and 100 MPa, measured considering the nominal contact area (25 cm^2) of the forcing blocks. Shear deformation is induced at constant loading point velocity of 1 µm s^{-1} for a fixed amount of slip of 13 mm. This stage is designed to produce a variety of fault fabrics (e.g., Hobbs & Ord, 2014), also referred to as textures (e.g., Sibson, 1977), which develop as a function of the stress conditions. We will use "fabric" to broadly include the geometric properties of fault rocks (e.g., grain size) and their spatial distribution (e.g., degree of localisation and/or foliation development).

Before commencing RA stage, the vertical stress is removed, then the normal stress is brought invariantly to 35 MPa and the vertical ram is de-stiffened by inserting a plexiglass prism (vertical spacer) in series with the central forcing block (stiffness k = 2.96 MPa mm^{-1}, Figure 1b). This procedure is performed in a short time frame (at most, 16 min). Then, during RA stage, the samples are sheared at the same constant velocity of 1 µm s^{-1}. Under these conditions, Scuderi et al. (2020) observed that the critical stiffness (k_c) of the anhydrite and dolomite mixtures is close to that of the de-stiffened loading ram ($k/k_c \approx$ 1), promoting nearly unstable conditions (e.g., Leeman et al., 2016) and giving rise to slow stick-slip events. We assume that when the k/k_c ratio approaches 1, thus lying in proximity of the bifurcation of the stability criterion (Gu et al., 1984), small differences in the mechanical properties and fabrics of the fault may affect the bulk frictional response. Therefore, by choosing the same experimental conditions during RA stage, we can isolate the effect of fault fabric generated at different normal stresses during TX phase on the slip behavior.
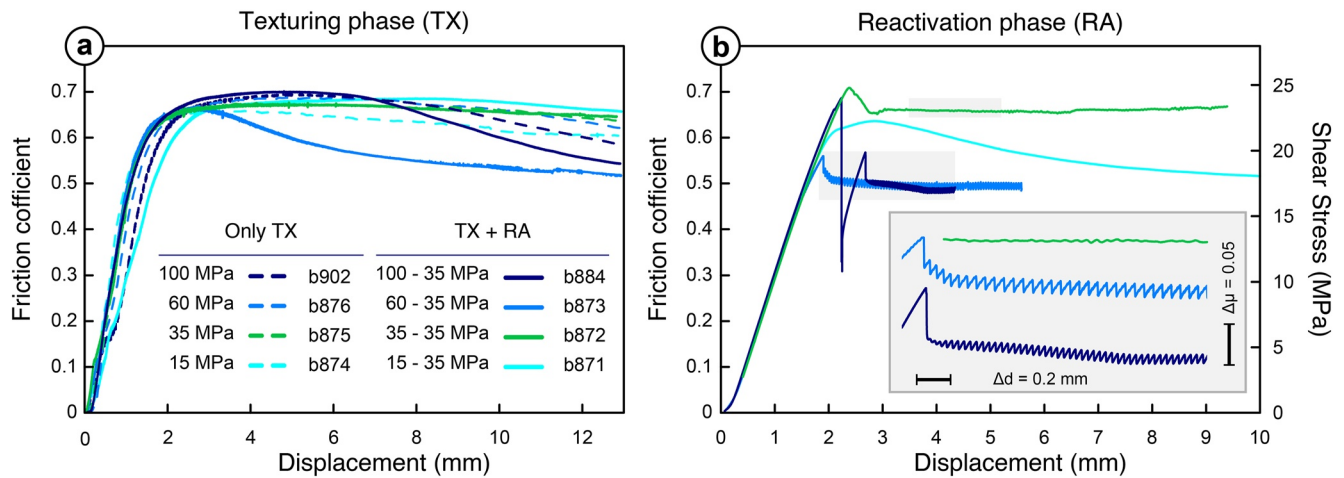
Figure 2. Evolution of friction (shear stress normalized by the normal stress) with displacement for both texturing (a) and reactivation (b) phases. Inset of (b) enlarges the shaded areas of experiments showing unstable behavior. Refer to legend in the inset of (a) for both panels.

To understand the micro-mechanisms at the origin of the observed fault slip behavior, for each normal stress, experiments were repeated but stopped at the end of TX phase for sample recovery. We assume that faults formed at the same experimental conditions should develop the same fabric. Thus, microstructures recovered at the end of each TX phase can be considered representative of the inherited fault fabric at the beginning of the following RA phase. This assumption holds because we observe comparable inherited structures when comparing TX with TX + RA (see Section 3.4), even though some variability is observed in the mechanical data (Figure 2). Both TX and TX + RA post-mortem samples were therefore recovered for microstructural investigation. Rock chips were embedded in epoxy, cut to expose a kinematic cross-section, and polished to mirror-like finish. We used scanning electron microscope (SEM) in backscattered mode for microstructural documentation.

In this paper, we will use "step-up" or "step-down" to refer to experiments where the normal load before the RA stage is less or greater than 35 MPa, respectively. Single experiments will be referred to with a simplified notation of their normal stress history (e.g., 15→35, experiment with TX at $\sigma_N = 15$ and RA at $\sigma_N = 35$).

3. Results

3.1. Mechanical Data

Figure 2 reports the evolution of the friction coefficient ($\mu = \tau\sigma_N^{-1}$, where τ is the shear stress) with displacement. During TX, the fault loads elastically until friction starts evolving nonlinearly (<1.5 mm of displacement) to peak values as high as ∼0.7 (2–5 mm). Subsequent strain-weakening shows a range of variability between experiments, with friction values ranging between $0.5 < \mu < 0.7$. As expected, slip is stable throughout TX phase (because $k/k_c \gg 1$). During the following RA phase, after the vertical ram is de-stiffened, faults load linearly with measured stiffness of 0.337 (15→35), 0.356 (35→35), 0.360 (60→35), and 0.366 (100→35) mm^{-1} (Figure S18 in Supporting Information S1). Only the 15→35 experiment follows with a smooth transition to inelastic deformation, peak friction lower than that recorded at the end of TX phase, and stable strain-weakening behavior. For all of the other stress conditions, friction reaches peak values higher than those recorded at the end of their TX stage. The fault sliding at constant normal load (35→35) reactivates at peak friction $\mu \approx 0.71$ with gradual strain-weakening to $\mu \approx 0.68$. Friction remains overall constant during slip, but shows small, irregular fluctuations ($\Delta\mu \ll 0.01$) indicative of small stick-slip events at the bifurcation between stable and unstable behavior. Differently from the other experiments, 35→35 displays reproducible higher friction coefficients upon re-shear (Figure S17 in Supporting Information S1).

Step-down stress experiments (60→35 and 100→35) are characterized by one or more sudden friction drops (RA events) that interrupt the elastic loading phase. Subsequent slip is markedly unstable and manifests for both
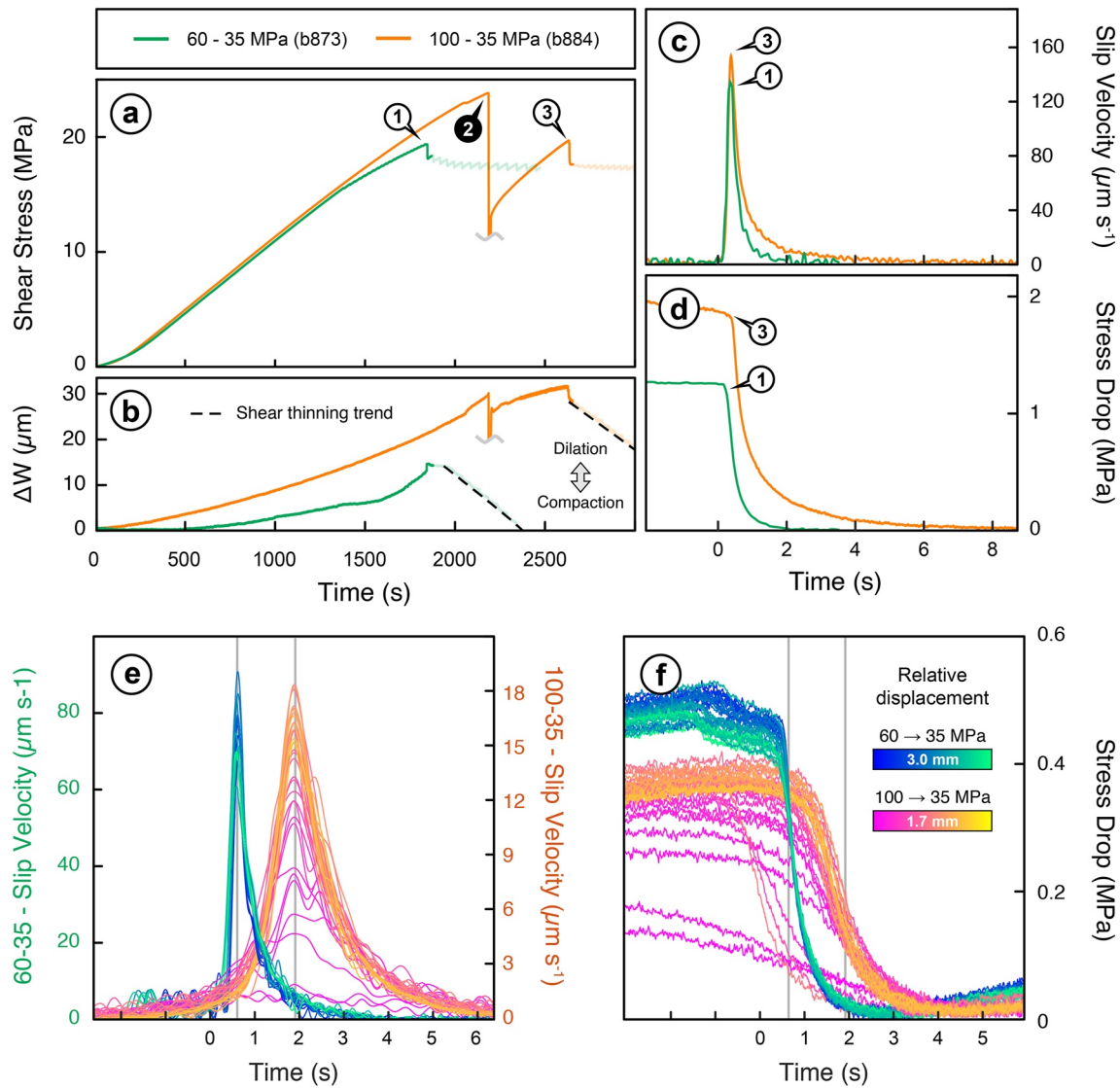
Figure 3. Detail of the mechanical behavior of reactivation (RA) phase of experiments 60→35 and 100→35. (a) Loading phase preceding stick-slip events, characterized by dilatant behavior recorded by the variation of the layer thickness, ΔW (b). The loading phase is interrupted by main stress drop events (1–3). Detail of the slip velocity function (c) and stress drop (d) of two main events (1, 3). Both events are characterized by asymmetric slip velocity function. Stick-slip events: detail of the slip velocity (e) and stress drop (f) of in function of relative loading point displacement. 60→35 events are asymmetric, while 100→35 events have longer duration and Gaussian-type velocity distribution in time. 60→35 events reach higher peak velocity (note the different scale). Curves in (e and f) are aligned using peak velocity as reference in time (gray line).

experiments with regularly spaced slow stick-slip events (Figure 2a, inset). In the following, we will describe the characteristics of the RA events and the stick-slip instabilities.

3.2. RA Events

Both step-down stress faults (60→35 and 100→35) are reactivated with relatively large stress drops (distinguished by subsequent smaller stick-slip events) after an almost entirely linear (elastic) loading phase, when faults are locked ($v \approx 0$) and display monotonic dilatant behavior (Figure 3b).

The 60→35 shear stress suddenly drops after reaching a peak stress of 19.5 MPa (Figure 3a). Peak slip velocity of 135 μm s^{-1} is reached after an acceleration time (T_{acc}, defined as the time to reach the peak) of 0.4 s and is followed by a progressive, concave deceleration to the background sliding velocity and residual stress. This event
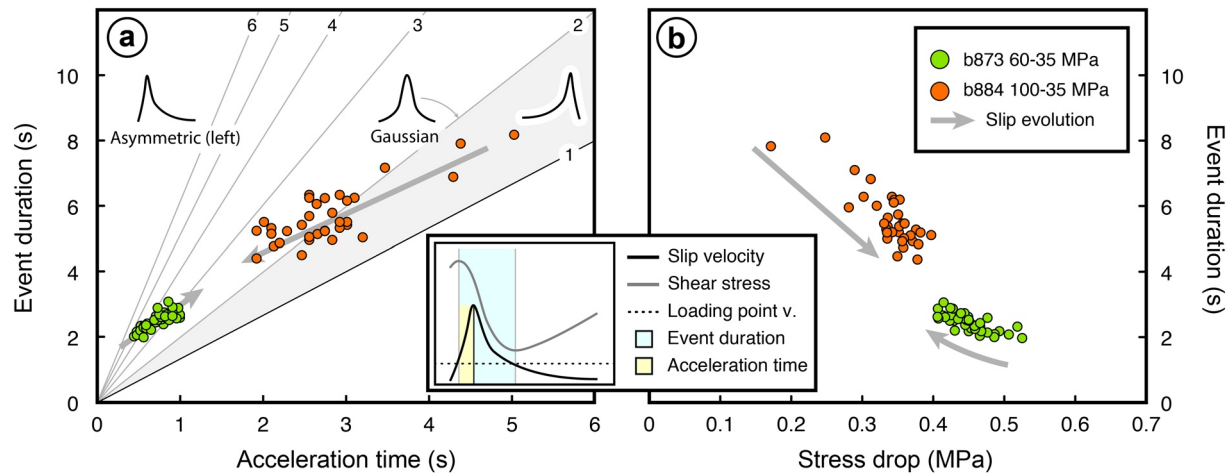
Figure 4. Event duration as a function of acceleration time (a) and stress drop (b) of stick-slip events for 60→35 (green) and 100→35 (orange) experiments. Oblique lines in (a) and associated numbers indicate the ratio between event duration and acceleration time, defining the asymmetry of the slip velocity function. Events lying on the line with slope equal to two are symmetric. In the schematic inset, the duration of the event is the time (azure shading) during which the slip velocity is above the load-point velocity and acceleration time is defined as the time (yellow shading) from initiation of the dynamic slip to the achievement of peak slip velocity.

defines a strongly asymmetric evolution of slip velocity with time (slip velocity function). Even if this time history represents the average behavior of the entire laboratory fault (considered as a point source), it resembles source-time functions observed in 2D dynamic rupture modeling and proposed in kinematic and pseudo-dynamic modeling (Mena et al., 2010; Tinti et al., 2005) due to its strong theoretical basis (e.g.,Kostrov, 1974; Yoffe, 1951). The total duration of the event, defined as the weakening time from peak to minimum stress (see inset of Figure 4), is $T_w \approx 2$ s for a total shear stress drop of 1.25 MPa.

The first RA of 100→35 occurs at peak shear stress of ~24 MPa ($\mu \approx 0.69$, Figure 3a). A large stress drop of >10 MPa is accompanied by fast slip velocity (lower estimate, > cm/s) and sharp, audible acoustic energy radiation. Due to the short duration of the event ($T_w < 0.01$ s) and a limited data acquisition rate we could not retrieve a reliable slip velocity function but, from a repeated run (Figure S16 in Supporting Information S1), we estimate a peak slip velocity of >4 m/s (with associated total slip of ~1 mm and shear stress drop of ~20 MPa). A second event follows the elastic re-strengthening to $\tau = 19.87$ ($\mu \approx 0.57$, Figure 3a). Again, the slip function is clearly asymmetric and similar in amplitude and duration to the RA event of the 60→35 experiment (Figure 3c). Peak velocity is ~154 μm s^{-1}, duration $T_w \approx 6$ s and stress drop 1.9 MPa.

3.3. Stick-Slip Instabilities

After RA, the friction of step-down stress experiments approaches values comparable to those of TX stage ($\mu \approx 0.5$) and manifests marked unstable behavior with stick-slip events. Nonetheless, the series of events belonging to the 60→35 and 100→35 experiments are mechanically distinct.

Each 60→35 stick-slip event is characterized by an asymmetric slip velocity function (Figures 3e and 4a). The acceleration time T_{acc} is less than 33% of T_w, which evolves with strain from 1.9 to 3.1 s (Figure 3a and green dots in Figure 4a). The shear stress drops rapidly at the beginning of slip acceleration then decays gradually with a concave slope (Figure 3f). Peak slip velocity (varying between 60 and 90 μm s^{-1}, Figure 3e) and stress drop (0.41–0.52 MPa, Figure 4b) slightly decrease with accumulated displacement and event duration.

100→35 stick-slip events, differently from the 60→35 events, follow a symmetric, Gaussian-shaped velocity function (T_{acc} is approximately half of T_w) and have longer duration T_w, ranging between 4.4 and 8.2 s (Figures 3e and 4a). Each event is preceded and followed by creep motion that consists of slip velocities smaller than the loading point velocity, for a total duration > T_w. The transition from and to creep velocities complete a symmetric Gaussian function. Differently from 60→35, the experimental fault is never locked and slips at detectable velocity, down to 0.1 μm s^{-1}, in the interseismic periods. The stress drop ranges between 0.13 and 0.4 MPa (Figure 4b)

and follows a smooth, sigmoidal function (Figure 3f) in agreement with the evolution of slip velocity (Figure 3e). Peak slip velocity (up to 19 µm s⁻¹) slightly increases with displacement (Figures 3e and 3f), and the stress drop is inversely correlated to the duration of the event (Figure 4b).

3.4. Microstructures

Given that RA stage of each experiment is performed at the same experimental conditions, we infer that the different properties of the laboratory earthquakes can be attributed to the inner fault texture that was formed during TX stage. The microstructural investigation has been carried on polished cross-sections of all post-mortem (TX and TX + RA) samples using a JEOL JSM 6500F SEM (equipped with a field emission source) in backscattered electron mode. For optimal imaging, we used a voltage of 15 keV and a working distance of 10 mm. Panoramas of the entire cross-sections showing the location of panels of Figure 5 and enlarged close-up images are included in Supporting Information S1.

At σ_N = 15 MPa TX deformation is localized in Riedel (R-) shears and a thin (∼100 µm) boundary-parallel shear band (Figure 5a) where most deformation is inferred to occur, that is, the principal slip zone (PSZ). Outside the PSZ and the R-shears the material is nearly undeformed. These regions represent low strain domains that were mostly active before localization in the PSZ. Grain size reduction within the PSZ (Figure 5b) produces a load-bearing framework of still relatively coarse, angular to sub-angular clasts (∼10 µm) coexisting with a finer matrix (<5 µm). During RA, the PSZ is dominated by smaller (<10 µm) and more rounded clasts, which embed fewer angular porphyroclasts (Figure 5d). Cataclastic processes are locally enhanced within discontinuous Y-shear bands (Figure 5d, orange arrow).

At σ_N = 35 MPa R-shears have reworked a larger volume of the fault (Figure 5e). One or more discontinuous, boundary-parallel PSZs are contained within a wider comminuted zone (>200 µm), which shows irregular boundaries and gradual grain size transition toward the low strain domains. Cataclastic processes also penetrate between the indenters forming asymmetric embayments (white arrows in Figure 5e and Figure S10 in Supporting Information S1). The porphyroclasts found within the PSZ (dominantly dolomite) are smaller (up to 10 µm), sub-angular and more spaced with respect to those formed at lower stress (Figure 5f). Here, the matrix is finer and has an abundant fraction below 1 µm. No substantial change in texture is observed after reactivation (RA stage, Figure 5g) except for a slightly more comminuted grain size in well-developed PSZs (Figure 5h).

The boundary-parallel shear band formed at σ_N = 60 MPa is irregular, with pronounced foliated S texture (Figure 5i). A single, non-foliated PSZ (width ≈ 100 µm) is found in proximity of the sliding forcing block. Here the grain size is extremely reduced (Figure 5j) and is composed of abundant matrix of round nanograins (<1 µm) and dispersed sub-angular porphyroclasts of dolomite (most <5 µm). During RA, cataclastic processes have reworked the PSZ and the neighboring low strain domains producing several fine-grained layers with thickness <30 µm (Figure 5k). These layers produce local sharpening of the boundaries between low and high strain domains (Figure 5k, orange arrow). Low-strain domains (white star in Figures 5i and 5k) are now subject to intense pluck-out of grains during polishing. PSZ is less resistant to erosion during the lapping procedure (see the intense pluck-out in Figure 5l) but preserves the same degree of localisation (∼100 µm) and grain sizes observed before RA (Figure 5j).

At σ_N = 100 MPa (Figure 5m) the overall architecture is similar to that formed at 60 MPa (Figure 5i). However, the low strain domains are pervasively foliated (Figure 5m) for a thickness locally exceeding 700 µm. A single, thin (∼50 µm) PSZ nucleates close to the indentation of the slider (Figures 6a and 6d). Within the PSZ we observe that the material has undergone extreme grain size reduction as most grains have sub-micron diameter, especially the anhydrite fraction (Figure 6d and Figure S14 in Supporting Information S1). In general, the PSZ fabric consists of low-porosity and cemented nanogranular aggregates (Figures 7c and 7f). Larger grains embedded in the fine matrix show fractures healed with light-colored phase (anhydrite, arrow in Figure 7f), forming thin films, and some are elongated in ribbon-like shapes (Figure 6d). Low strain domains show a pervasive S-C' foliation (Figure 7b). Here, some grains are finely polygonized (Figure 7e), indented by neighboring angular grains (Figure 7e) and present an elongated, ribbon-like, habit (Figures 6a, 7b, and 7d). The S-fabric is decorated by trails of fine-grained material, both anhydrite and dolomite, with grain size similar to that of the PSZ (Figure 7d). The samples removed at the end of TX stage are substantially more resistant to sampling damage than the other collected samples and the entire thickness is easily preserved. No fabric changes are observed at the scale of
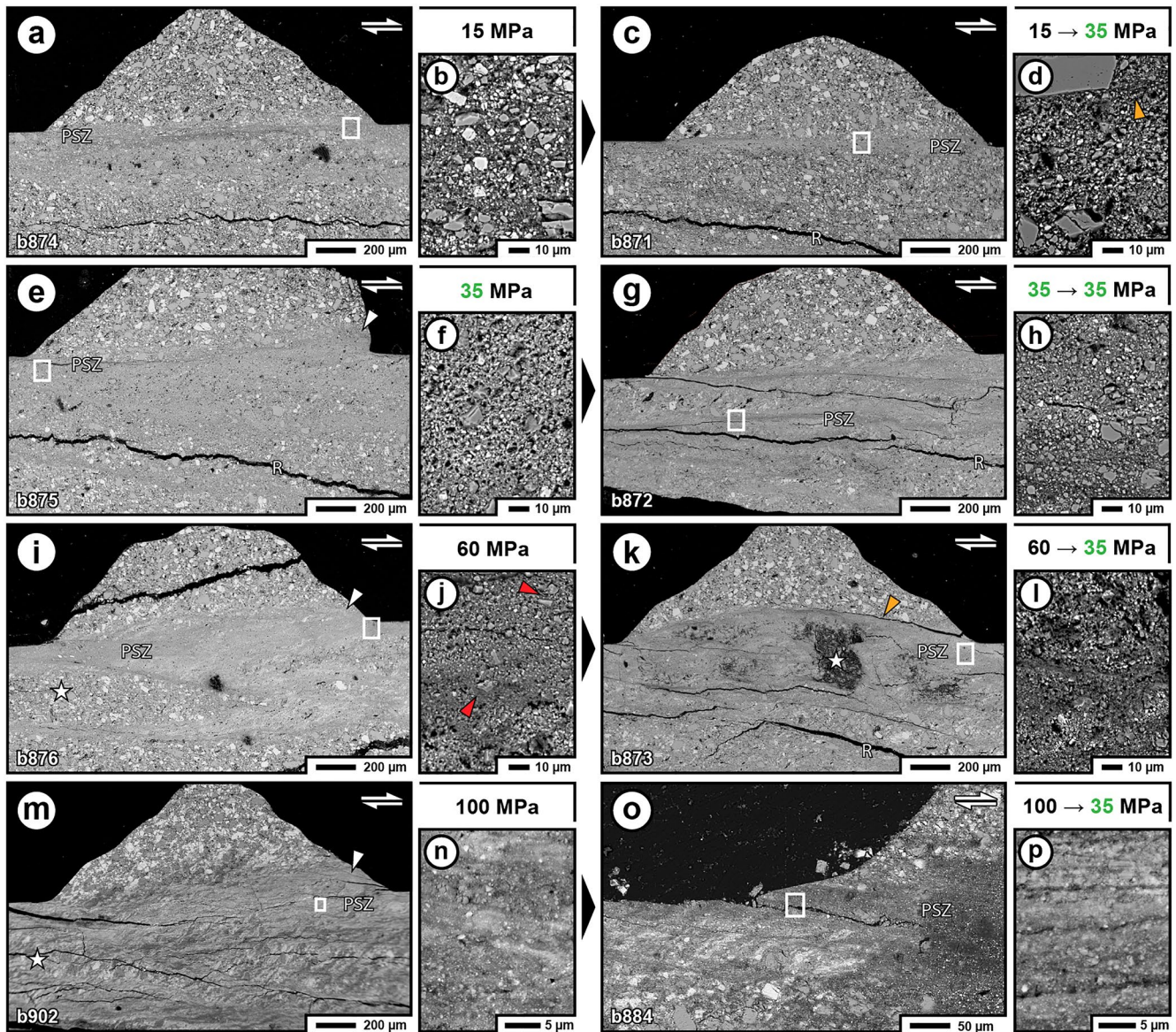
Figure 5. Backscattered SEM images of the experimental faults (large frames) in proximity of the principal slip zone (PSZ), and associate close-ups (small frames) of the areas enclosed by white boxes, which show the fine material of the PSZ. Fault fabrics produced during TX and RA phases are on the left and right hand side columns, respectively. Legend: PSZ, principal slip zone; R, Riedel shear bands; *white arrows*, damage zone embayment; *orange arrows*, shear localisation and truncation; *red arrows*, porphyroclasts; *star*, isolated low-strain domains. The locations of these close-ups are reported in Figures S1–S8 in Supporting Information S1. Enlarged versions of all panels are reported in S9–S12 in Supporting Information S1.

the sample after RA (Figure 5o). However, recovery of full-thickness of RA samples is almost impossible due to splitting along the PSZ. The PSZ and its boundaries, where preserved, are prone to scouring during sample preparation and present damage (Figure 6c). These areas are formed by relatively large, angular aggregates of abundant sub-micron sized particles and larger angular clasts (Figures 6c and 6f), and disaggregated material of the same nature. Locally, the embrittled volume is limited by a sharp, flat truncation from the undamaged low strain domains (Figure 6c). An additional microstructure is recovered immediately after the first seismic RA event (experiment b1001, Figure S16 in Supporting Information S1). The narrow PSZ shows substantial less reworking than that of b884, while damage in form of Riedel-oriented cracks is observed in the low strain domains (Figure 6b). In PSZ, sub-angular grains of dolomite are finely dispersed in an anhydrite matrix and show virtually no porosity (Figure 6e). These grains are almost entirely below the micron scale, except for some rounded porphyroclasts, and present a faint oblique fabric (Figure 6e). Locally, round porosity at the sub-micron
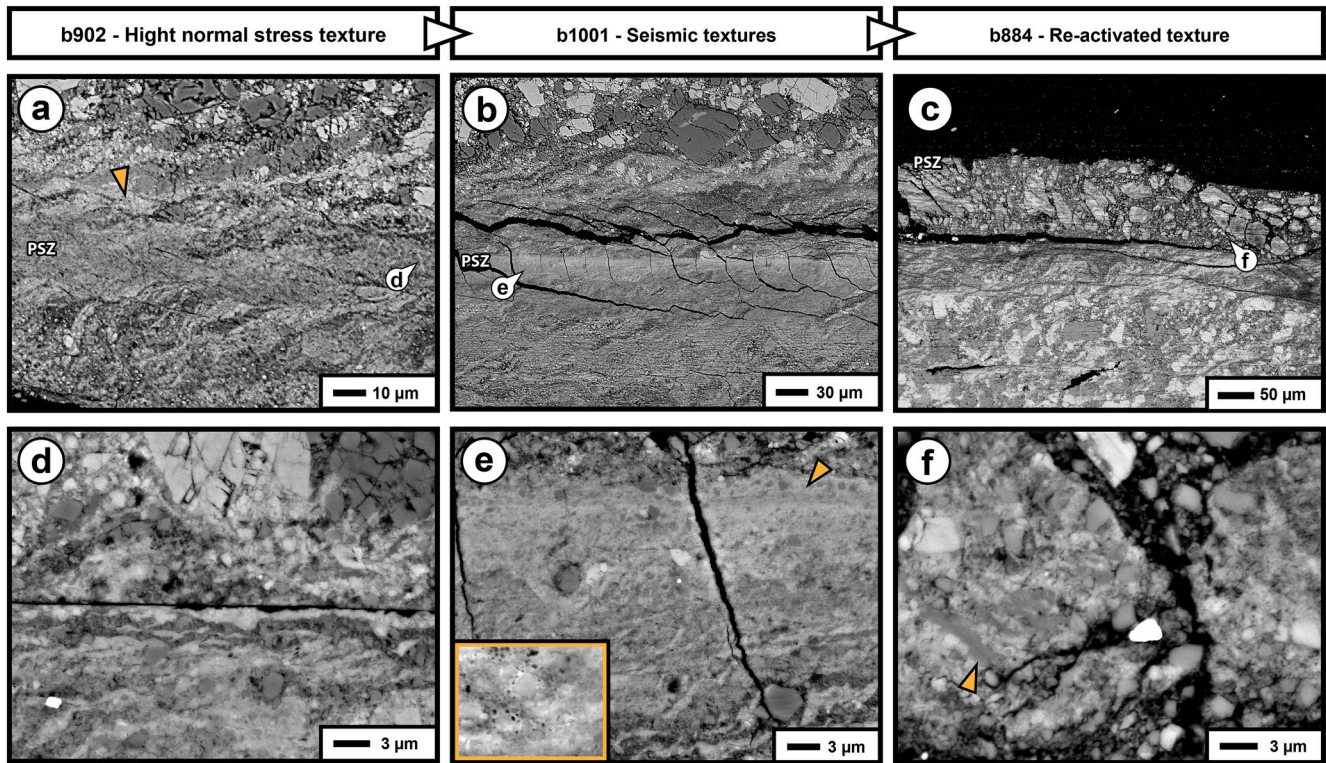
Figure 6. Detail of the principal slip zone (PSZ) and neighboring regions of experiment performed at 100 MPa (a) and reactivated at 35 MPa (b–c). The sense of shear in all panels is dextral. Panels (d– f) present magnifications of the regions indicated by the balloons. (a) The principal slip zone shows extreme grain size comminution (d), low porosity and gradual transition of grain size and foliation angles toward the low strain domains (arrow). No cracks are observed around the PSZ. (b) Textures recovered immediately after the first reactivation with seismic slip velocities present a narrow PSZ with extremely fine, homogeneous grain size (e). Inner fabric shows the loss of the foliation observed during TX phase (compare panels e and d) but preserves rare porphyroclasts and a faint oblique foliation. The area indicated with an arrow and enlarged in the inset (field of view: 4 μm) shows rounded nano-porosity in the anhydrite matrix, possibly indicating thermal decomposition. Riedel-oriented fractures populate the foliated area outside the PSZ, which is in turn fragmented with sub-vertical fractures. (c) After reactivation and following several stick-slip cycles, the PSZ is completely reworked into sub-micron sized material (see also Figure 5p). Due to its fine grain size and high porosity, the PSZ is almost impossible to recover. Larger fragments of foliated materials are preserved close to the PSZ and correspond to the damaged zones in proximity of the PSZ (as in panel (b)).

scale hosted by the fine anhydrite matrix (inset of Figure 6e) suggests thermal decomposition processes (e.g., Han et al., 2010). Similar PSZs, composed by extremely fine grain sizes, low porosity and oblique foliation, were observed in high velocity shear experiments performed in the same materials (Pozzi et al., 2021). This finds good agreement with the mechanical results that indicate rapid, seismic slip.

4. Discussion

Different deformation mechanisms and associated rock types (e.g., cataclasites and fault gouges) have been invoked to play a primary role in earthquake processes (e.g., Sibson, 1977). Cataclastic processes are prominent in natural faults (Sibson, 1977) and they have been extensively simulated in the laboratory for the study of earthquake physics. Furthermore, faults within the seismogenic layer also bear widespread evidence of fluid-rock interactions (e.g., Collettini et al., 2019; Cox, 2016; Sibson, 1992; Tarling et al., 2019). These chemical processes are known to promote strength recovery and healing in granular materials (Angevine et al., 1982; Karner & Marone, 1998; Tenthorey et al., 2003), suggesting that the processes of shear failure in lithified faults are also relevant to earthquake nucleation (Cox, 2017; Ikari & Hüpers, 2021; Ikari, Niemeijer, & Marone, 2011; Muhuri et al., 2003).

The studies of ancient faults exposed at the surface together with laboratory experiments indicate the crucial role of both frictional and chemical processes in affecting fault slip behavior. In this work, we show that fault slip behavior is intimately connected with the rock fabric of the simulated fault, and it is influenced by the faults'
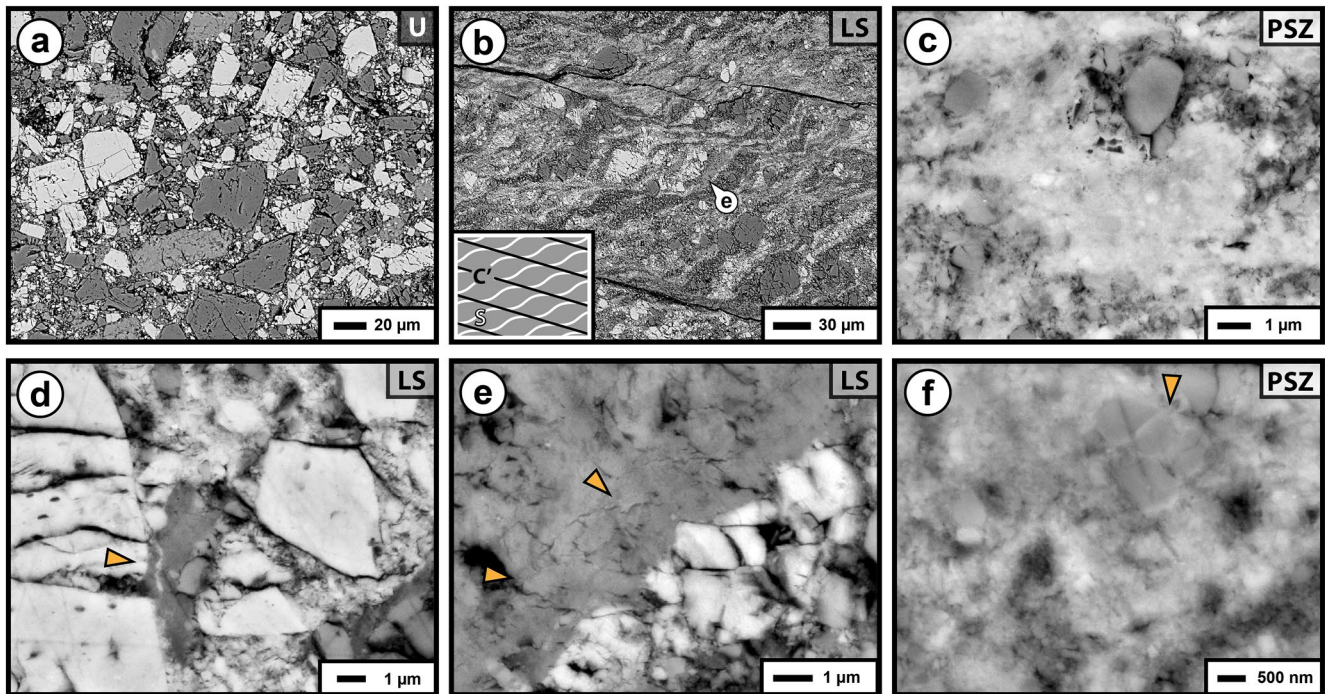
Figure 7. Close-up of microstructures observed in experiment b902 (100 MPa texturing). The sense of shear in all panels is dextral. Labels in the upper right corner indicate the relative location of microstructures: U, nearly undeformed region preserved within the indentation with the forcing blocks; LS, foliated low strain domains, PSZ, principal slip zone. (a) Grains of dolomite (dark gray) and anhydrite (light gray) not affected by shear deformation. Grain size reduction is local and heterogeneous. (b) Low strain domains show dominant brittle deformation and s-c' fabric highlighted by trails of cataclastic products and ribbon-like clasts (close up in (e)). (c) Low-porosity aggregate of sub-micron sized grains (dominantly anhydrite) that envelope larger sub-angular clasts of dolomite. (d) Ribbon-like dolomite grain enclosing an elongated anhydrite ribbon (arrow). (e) Anhydrite clasts indenting a dolomite clast within the low strain domains; ribbon-like grains show frequently an inner polygonal pattern highlighted by jigsaw micro-cracks (arrows) that isolate small particles of grain size comparable with the PSZ's grains. (f) Thin films of anhydrite cementing fragmented dolomite clasts with nanometric displacement (arrow).

deformation and healing (frictional and chemical) history. In the following sections is discussed first how fault fabric controls the slip behavior upon RA, and second how the dynamics of repeating slow stick-slip events are modulated by fault fabric.

4.1. Frictional Stability During RA

Texturing phase, TX, at four normal stresses (σ_N = 15, 35, 60, and 100 MPa) has produced different fault fabrics that, when reactivated at the same experimental conditions (close to the frictional stability transition previously documented by Scuderi et al., 2020), present a different slip behavior.

The re-shear stage, RA, of a fault brought close to the stability transition from low to higher stress, (15→35) favors stable sliding. This regime is linked to the deformation of a principal slipping zone, PSZ, composed of coarse and angular grains, which experience further grain size reduction throughout the RA stage. Progressive localization along thin but discontinuous *y*-shear bands is also observed (Figure 5d). This suggests that the fabric of the PSZ is not in equilibrium with the new stress conditions and frictional stability is promoted by means of further shear compaction and cataclasis (e.g., Niemeijer et al., 2010). The wide grain size distribution and angularity of clasts also contribute to suppress the frictional instability (Anthony & Marone, 2005; Mair et al., 2002; Marone & Kilgore, 1993). Nevertheless, stick-slip motion was observed at σ_N = 35 MPa in (initially coarser) anhydrite-dolomite powders (Scuderi et al., 2020). We therefore do not exclude the occurrence of instabilities at higher strains (e.g., Mair & Marone, 1999; Niemeijer et al., 2010; Scuderi et al., 2017), as observed in the case of the 35→35 experiment in this data set (Figure 2b).

Marked frictional instabilities are in turn observed during RA at "step-down" stress conditions. TX performed at σ_N = 60 MPa and σ_N = 100 MPa promotes moderate (1.2 MPa) to large (>10 MPa) stress drops upon RA,

respectively. These events are characterized by an asymmetric slip velocity function (Figure 3c) and fast acceleration to peak velocity. Scuderi et al. (2017) have observed in similar tests that, after reduction of the normal stress (from 35 to 15 MPa), larger stick-slip instabilities can result from the reduced loading stiffness, which is acquired at large normal stresses and is maintained when the normal stress is reduced. This is not observed in our experiments, where the loading stiffness (measured on the linear slope of the initial loading to peak friction during RA) is comparable for both 100→35 and 60→35 (Figure S16 in Supporting Information S1). The respective RA events are in fact substantially different (slow slip vs. seismic slip). Some variations of kc—which is not measurable during RA—might affect the stability of the fault but are unlikely to explain the large stress drops observed here (see Tinti et al., 2016).

The re-activation events of 100→35 and 60→35 are characterized by velocities far exceeding the loading point velocity (values $\gg$ 1 µm/s) and are accompanied by marked dilation upon initiation of on-fault slip (Figure S16 in Supporting Information S1 and Figure 3b). This behavior is similar to re-sliding in halite experiments when chemical healing affects the frictional behavior of the experimental fault (van den Ende & Niemeijer, 2019). The 35→35 experiment, on the other hand, reactivated at velocities close to the loading point velocity and displays shear-thinning trends (Figure S16 in Supporting Information S1). These findings suggest that chemically assisted healing, together with friction, may play a fundamental role in enhancing dynamic instabilities.

Evidence of healed fault rocks is found in our experiment performed at high TX stress (100 MPa). The low porosity of the PSZ (Figures 7c and 7f), cemented fractures (arrows in Figure 7f) and ribbon-like, polygonized grains (Figures 6d, 7d, and 7e) suggest the activity mass transfer processes. Extreme grain size reduction (<1 µm) and polygonization of grains (Figure 7e) also points to enhanced intragranular plasticity (e.g., Verberne et al., 2019). We infer that these processes, which are efficient at high stresses and in presence of fluids (e.g., water adsorbed at 100% humidity conditions), promote frictional healing due to a severe reduction of porosity and local cementation of anhydrite (e.g., chemically assisted healing, Bos et al., 2000), active even during deformation (as suggested by the foliated texture of the PSZ, Figure 6d).

We therefore propose that the overconsolidated (see Marone & Scholz, 1989) and healed fault materials in the PSZ embrittle and dilate upon re-shear (Figure 3a), allowing the entire fault to yield through fast (first event of 100→35) and/or slow slip events (first event of 60→35 and s event of 100→35). The fracturing of the fault is indeed evidenced by the damage at the PSZ boundary (Figure 6b), which is composed of dismembered and relatively large, angular aggregates of abundant sub-micron sized particles (Figure 6f). This substantial reworking of the PSZ is likely to occur almost entirely during the RA events since they are mechanically distinct from the following stick-slip events and are non-repeatable. Our results are similar to experiments designed to reactivate a natural cemented carbonate fault showing values of apparent peak friction of $\mu = 0.95$ that directly precede a shear stress drop of 3.3 MPa (Carpenter et al., 2014). Other experiments on crystalline basement rocks show that fault welding by pseudotachylytes formation gives important fault frictional healing preventing further shear on the same slip surface (Hayward & Cox, 2017; Mitchell et al., 2016). In contrast, RA of our experimental faults occurs along pre-existing discontinuities (i.e., the boundary-parallel foliation, Figure 6d) and reworks the PSZ, with the effect of re-localizing deformation and increasing the porosity (e.g., Figure 6c). Similar results were also obtained in experiments performed on carbonate fault gouges (Smith et al., 2015). These events are fundamental to "unlock" the fine-grained and rounded material within the PSZ, as discussed in Section 4.2.

Unstable RA is only met when $k/k_c \sim 1$ and with step-down stress RA, therefore it is natural to question in what geological contexts such conditions can be attained. The elastic dislocation theory (Eshelby, 1957) coupled with rate and state friction modeling indicates that the stiffness, k, for a confined slip is directly proportional to the rigidity and inversely proportional to the size of the slip patch (Dieterich, 1979). Therefore, in natural faults, for fixed dynamic conditions (related to the dynamic parameters that define kc), the local stiffness around it (k) gets smaller as the fault patch prone to dislocate becomes bigger, until the condition to satisfy the instability transition are reached (Liu & Rice, 2007; Segall et al., 2010). In the laboratory experiments, it is impossible to increase the size of the slip patch due to the sample limit, thus the unstable condition can be achieved in a similar way by decreasing the stiffness of the machine. In addition, the stability condition $k/k_c \sim 1$ in natural faults can be obtained for increasing kc values due to fault zone heterogeneity (e.g., Ampuero & Rubin, 2008; Barbot, 2021; Cattania & Segall, 2021). Besides, RA by step-down stress conditions corresponds to a reduction in normal stress during fault loading and is achieved every time fluid pressure increases (Sibson, 1992), and this condition is met in numerous tectonic contexts. Along subduction zones fluid overpressure likely forms from dehydration

reactions (Peacock & Wang, 1999) and is supported by geophysical (Audet & Bürgmann, 2014) and geological investigations (Behr et al., 2018; Fagereng et al., 2010). Moreover, fluid pressure development and induced seismicity can be observed following the modern techniques for energy production (e.g., McGarr et al., 2015). Finally, the recent major earthquakes occurred in central Italy, which nucleated on the same fault rocks tested here (Barchi et al., 2021), are likely triggered by fluid overpressure (Chiarabba et al., 2020; Miller et al., 2004).

4.2. The Mechanics of Slow Frictional Sliding

Our experimental procedure was specifically designed to test the hypothesis of whether fault slip behavior (i.e., slow or fast) is controlled by the inherited fault rock structure. It is well documented that the degree of strain localization and strain rate distribution, physico-chemical processes and grain size, amongst many other factors, can influence second order variations in the frictional response of the fault gouge, controlling the rate and state frictional properties, resulting in potential different fault slip behaviors (e.g., Beeler et al., 1996; Leeman et al., 2016; Mclaskey & Yamashita, 2017; Shreedharan et al., 2020). Such differences measured during our laboratory experiments cannot be fully reproduced by a simple spring slider model (Beeler et al., 2014), and need some variability of dynamic parameters in time (e.g., Im et al., 2020) or in space (e.g., 2D dynamic modeling). Following the framework built by Scuderi et al. (2020) for anhydrite-dolomite mixtures, we confirmed that the transition from stable to unstable slip is primarily controlled by the stiffness ratio, that is, $k/k_c \sim 1$ that we obtain at $\sigma_N = 35$ MPa by adding a spring in the loading system. However, here we have found that fault rock fabric has a profound effect on kinematics of slow slip events (i.e., the slip velocity time history).

After the RA described in the previous section, the faults slip unstably giving rise to rather regular, slow stick-slip events (Figure 4). This unstable behavior is modulated by the new boundary conditions and fabrics produced during the RA events. Deformation during stick-slip is accommodated within extremely comminuted, but porous PSZs (grains < 1 μm) with narrow grain size distribution. As the thickness of the PSZ of 100→35 is comparable to that of 15→35 (Figure 5), we suggest that localization is a required condition to develop the instability but has not the primary role in stick-slip behavior (i.e., the shape of the slip velocity and shear stress time functions) that instead seems to be promoted by the small grain size and roundness of grains formed only at high stresses, that is, 65 and 100 MPa (see e.g., Figures 5b and 5n). Nanosized particles may form strong force chains and hinder cataclastic deformation, which would promote stable slip (Anthony & Marone, 2005; Mair et al., 2002). For the two stick-slip series, here we propose a qualitative mechanical model that explains how the observed differences in slip velocity and stress drop evolution (Figures 3e and 3f) is modulated by the microstructures. During each stick-slip cycle we individuate three fundamental stages of fault motion (Figure 7): (I) interseismic period, (II) slip initiation and (III) dynamic slip.

100→35 PSZ is extremely homogeneous, composed of round grains smaller than 1 μm (Figure 8a). This minute grain size cannot be reduced by cataclastic means (e.g., Sammis & Ben-Zion, 2008). We, therefore, assume that they deform in a similar fashion to rigid bodies and that stick-slip events emerge due to the formation of force chains resisting the shear deformation (Figure 8a, Stage I, e.g., Mair et al., 2002). Failure of one or more chains transfers the stress across the layer to the next chain and dilates the fault, which starts creeping. When a critical stress state is reached, the entire fault yields following a cascading failure of force chains (Figure 8a, Stages II–III). We propose that the Gaussian velocity function and the sigmoidal shape of the stress drop is the result of the homogeneity of the PSZ. In support of this hypothesis, predynamic slip creep (v < loading point velocity) is associated with dilation and deviation from elastic increase of shear stress (Stage II in Figure 8a). This means that the transition to dynamic slip is continuous and is not triggered by the sudden failure of a stressed patch, but is linked to the critical density of particles (i.e., their compaction) and the number of particles in motion at a given time. Notably, the flex of the descending curve of slip velocity coincides with the onset of compaction, which suggests that the kinetic energy of particles is insufficient to work against the normal load, and slip is partly accommodated by densification.

Differently from 100→35, 60→35 PSZ contains several dispersed porphyroclasts (<5 μm, Figures 4j and 8b). Due to their separation, they may not form a homogeneous load-bearing framework but can "jam" within the granular flow via interaction of their local stress perturbation (Figure 8b, Stage I). This mechanism may form spaced, but strong force chains that, due to their width and smaller number of chained grains (Anthony & Marone, 2005), bear a larger stress. Failure of a single or multiple force chains is accompanied by rapid dilation (Figure 8b, Stage II) and leads to sudden acceleration of the fault due to the compliance of neighboring ones (Figure 8b, Stage III),
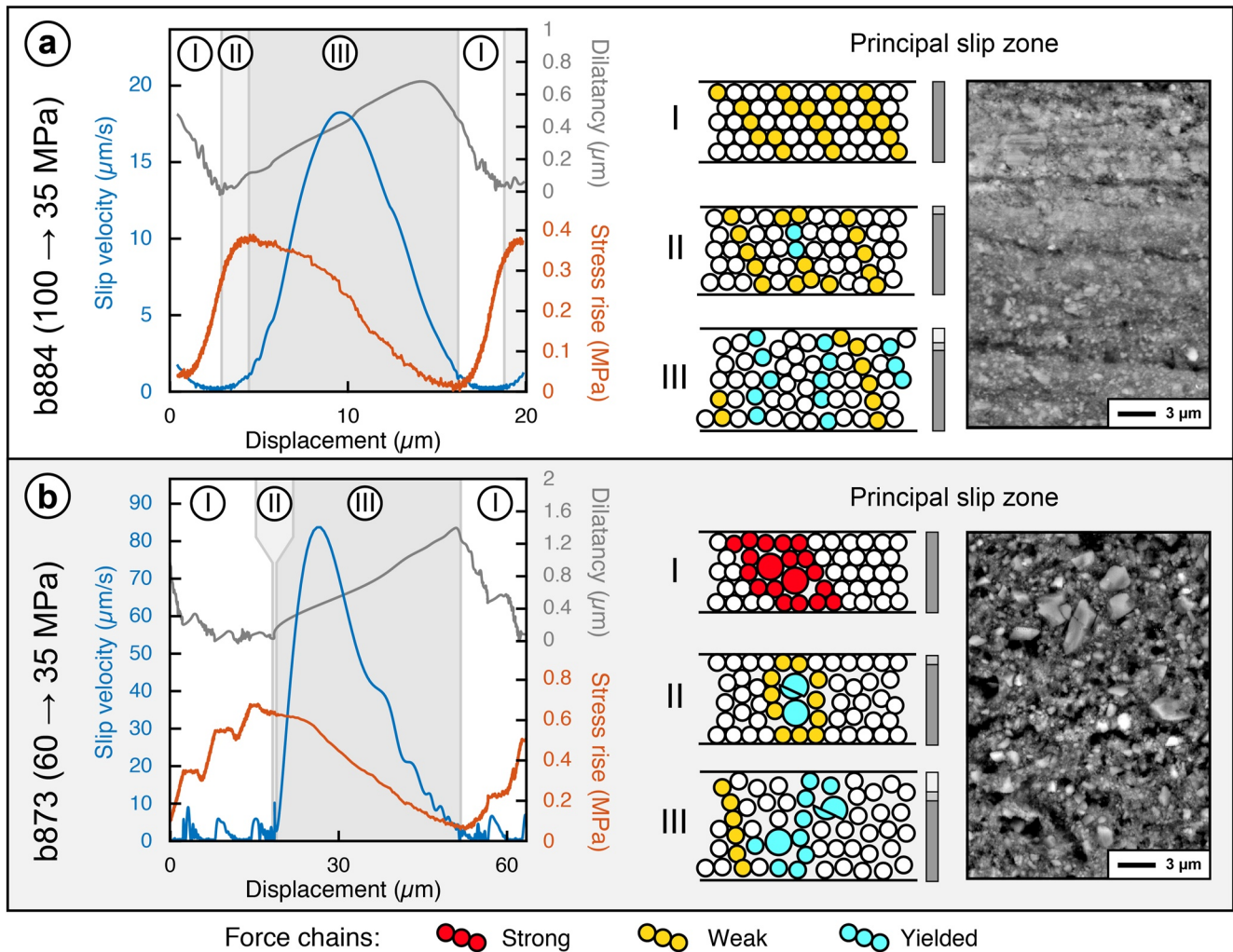
Figure 8. Interpretation of the nature of stick-slip events. Graphs show the mechanical properties of a sampled stick-slip event. The scheme on the right shows a conceptual arrangement of the grains and force chains within the principal slip zones (PSZ) throughout three stages (I–III) of the slip history: I—interseismic period; II—slip initiation; III—dynamic stage. Curves: blue—slip velocity; orange—stress evolution; gray—dilation, calculated by removing the shear thinning trend of the layer thickness variation. Gray bars: thickness and thickness changes of the deforming layer. The microstructural images (SEM backscattered electron images) show comparatively the different grain size contained in the respective PSZs.

which have a larger coordination number (i.e., number of small bridging particles; Anthony & Marone, 2005). Due to the absence of creep or dilation before the event (extremely short Stage II) we infer that the initial yield of the force chains is paroxysmal, possibly associated with brittle failure of porphyroclasts. Subsequent bulk grain size reduction slowly shifts the mechanical behavior —such as the shape of the slip velocity function—toward that of 100→35. This can explain the progressive reduction of asymmetry of the events' slip function and reduction in velocity with slip (Figures 3e and 4a). Assuming that at large displacement the cataclasis will continue to homogenize the grain size distribution in the PSZ, the slip velocity function can possibly evolve toward a Gaussian distribution in time such as that of 100→35 (see also evolution with slip in Figure 4).

The proposed mechanical model has been used to explain the observed differences in slip velocity time histories (Figure 2e). Stick-slips at 100→35 are characterized by creeping and acceleration to peak slip velocity followed by deceleration toward the background sliding velocity with a source time function that resembles a Gaussian slip velocity function. Stick-slips at 60→35 show instead a sharp slip acceleration followed by gradual slip deceleration. Similar differences in slip velocity functions have been observed in other laboratory experiments (Scuderi et al., 2020). In these experiments, a Gaussian slip velocity function is linked to slip along PSZ made of nanograins of quartz, whereas an asymmetric velocity function is recorded for slip along a heterogeneous and

foliated anhydrite/dolomite mixture. Our observations of both Gaussian and asymmetric slip velocity functions for the same anhydrite/dolomite mixtures confirm that fault fabric—and not only lithology—plays a key role in stick-slip behavior.

5. Conclusions

The texturing phase (TX) obtained at different levels of normal stress (15, 35, 60, and 100 MPa) allowed us to obtain a spectrum of fault microstructures. At high normal stress, deformation is localized along a low-porosity PSZ containing abundant nanograins, cemented fractures and ribbon-like grains, which are microstructures indicative of fault materials, which have undergone frictional and chemically assisted healing. After this phase we reloaded each fault at the same boundary conditions, $\sigma_N = 35$ MPa, chosen to approach the bifurcation of the frictional stability criterion, and noted that fault RA occurs by stable sliding in stress-up conditions (15→35) or by large instabilities in stress-down conditions (100→35 and 60→35). We propose that frictional and chemically assisted healing, which are efficient at high stresses, favored large (11 MPa at 100→35) and moderate stress drops (1.2 MPa at 60→35) during the RA at stress-down conditions. RA events are characterized by sudden acceleration to peak velocity and asymmetric slip velocity function. These observations suggest that the RA of healed faults may result in hazardous seismic failure when the normal load is decreased, for example, when fluid pressure increases during fault loading.

Fault fabric also plays a fundamental role in modulating the slip behavior after RA. Close to the stability transition (when the stiffness ratio is $k/k_c \sim 1$), a load-bearing framework of angular, relatively large grains (<10 μm) promotes stable sliding. PSZs formed predominantly by round, sub-micron sized material instead generate frictional instability, which manifests as slow stick-slip events with different dynamics. We propose that narrow distribution of grain sizes promotes dynamic slow slip events with Gaussian slip function, characterized by a smooth transition to interseismic creep. Instead, heterogeneities in the PSZ due to the presence of dispersed porphyroclasts (<5 μm), result in slow slip events with asymmetric slip function. Heterogeneity acts to produce inhomogeneous stress distribution and favors nucleation of faster-accelerating ruptures at the critically stressed patches.

Our laboratory data suggest that the characteristics of fault rocks play a key-role in the dynamics of earthquakes: chemically assisted frictional healing may facilitate earthquake nucleation whereas fault fabric controls slip velocity function and stress drop. In the light of these findings, further work is required to isolate and quantify the effect of chemical healing and its relevance in nucleation processes.

Data Availability Statement

Raw data files are available at https://zenodo.org/deposit/4940234.

References

Ampuero, J. P., & Rubin, A. M. (2008). Earthquake nucleation on rate and state faults—Aging and slip laws. *Journal of Geophysical Research: Solid Earth*, *113*, 1–21. https://doi.org/10.1029/2007JB005082

Angevine, C. L., Turcotte, D. L., & Furnish, M. D. (1982). Pressure solution lithification as a mechanism for the stick-slip behavior of faults. *Tectonics*, *1*, 151–160. https://doi.org/10.1029/TC001i002p00151

Anthony, J. L., & Marone, C. (2005). Influence of particle characteristics on granular friction. *Journal of Geophysical Research: Solid Earth*, *110*, 1–14. https://doi.org/10.1029/2004JB003399

Audet, P., & Bürgmann, R. (2014). Possible control of subduction zone slow-earthquake periodicity by silica enrichment. *Nature*, *510*, 389–392. https://doi.org/10.1038/nature13391

Barbot, S. (2021). A spectral boundary-integral method for quasi-dynamic ruptures of multiple parallel faults. *Bulletin of the Seismological Society of America*, *111*, 1614–1630. https://doi.org/10.1785/0120210004

Barchi, M. R., Carboni, F., Michele, M., Ercoli, M., Giorgetti, C., Porreca, M., et al. (2021). The influence of subsurface geology on the distribution of earthquakes during the 2016–2017 Central Italy seismic sequence. *Tectonophysics*, *807*, 228797. https://doi.org/10.1016/j.tecto.2021.228797

Bedford, J. D., & Faulkner, D. R. (2021). The role of grain size and effective normal stress on localization and the frictional stability of simulated quartz gouge. *Geophysical Research Letters*, *48*, e2020GL092023. https://doi.org/10.1029/2020GL092023

Beeler, N. M., Tullis, T., Junger, J., Kilgore, B., & Goldsby, D. (2014). Laboratory constraints on models of earthquake recurrence. *Journal of Geophysical Research: Solid Earth*, *119*, 8770–8791. https://doi.org/10.1002/2014JB011184

Beeler, N. M., Tullis, T. E., Blanpied, M. L., & Weeks, J. D. (1996). Frictional behavior of large displacement experimental faults. *Journal of Geophysical Research: Solid Earth*, *101*, 8697–8715. https://doi.org/10.1029/96JB00411

Behr, W. M., Kotowski, A. J., & Ashley, K. T. (2018). Dehydration-induced rheological heterogeneity and the deep tremor source in warm subduction zones. *Geology*, *46*, 475–478. https://doi.org/10.1130/G40105.1

Bos, B., Peach, C. J., & Spiers, C. J. (2000). Slip behavior of simulated gouge-bearing faults under conditions favoring pressure solution. *Journal of Geophysical Research: Solid Earth*, *105*, 16699–16717. https://doi.org/10.1029/2000jb900089

Brace, W. F., & Byerlee, J. D. (1966). Stick-slip as a mechanism for earthquakes. *Science*, *153*, 990–992. https://doi.org/10.1126/science.153.3739.990

Bürgmann, R. (2018). The geophysics, geology and mechanics of slow fault slip. *Earth and Planetary Science Letters*, *495*, 112–134. https://doi.org/10.1016/j.epsl.2018.04.062

Carpenter, B. M., Scuderi, M. M., Collettini, C., & Marone, C. (2014). Frictional heterogeneities on carbonate-bearing normal faults: Insights from the Monte Maggio Fault, Italy. *Journal of Geophysical Research: Solid Earth*, *119*, 9062–9076. https://doi.org/10.1002/2014JB011337

Cattania, C., & Segall, P. (2021). Precursory slow slip and foreshocks on rough faults. *Journal of Geophysical Research: Solid Earth*, *126*, 1–20. https://doi.org/10.1029/2020JB020430

Chen, J., & Spiers, C. J. (2016). Rate and state frictional and healing behavior of carbonate fault gouge explained using microphysical model. *Journal of Geophysical Research: Solid Earth*, *121*, 8642–8665. https://doi.org/10.1002/2016JB013470

Chester, F. M., Evans, J. P., & Biegel, R. L. (1993). Internal structure and weakening mechanisms of the San Andreas Fault. *Journal of Geophysical Research*, *98*, 771–786. https://doi.org/10.1029/92JB01866

Chiarabba, C., Buttinelli, M., Cattaneo, M., & De Gori, P. (2020). Large earthquakes driven by fluid overpressure: The Apennines normal faulting system case. *Tectonics*, *39*, e2019TC006014. https://doi.org/10.1029/2019TC006014

Collettini, C., Di Stefano, G., Carpenter, B., Scarlato, P., Tesei, T., Mollo, S., et al. (2014). A novel and versatile apparatus for brittle rock deformation. *International Journal of Rock Mechanics and Mining Sciences*, *66*, 114–123. https://doi.org/10.1016/j.ijrmms.2013.12.005

Collettini, C., Tesei, T., Scuderi, M. M., Carpenter, B. M., & Viti, C. (2019). Beyond Byerlee friction, weak faults and implications for slip behavior. *Earth and Planetary Science Letters*, *519*, 245–263. https://doi.org/10.1016/j.epsl.2019.05.011

Cox, S. F. (2016). Injection-driven swarm seismicity and permeability enhancement: Implications for the dynamics of hydrothermal ore systems in high fluid-flux, overpressured faulting regimes—An invited paper. *Economic Geology*, *111*, 559–587. https://doi.org/10.2113/econgeo.111.3.559

Cox, S. F. (2017). Rupture nucleation and fault slip: Fracture vs. friction. *Geology*, *45*, 861–862. https://doi.org/10.1130/focus0920172.1

De Paola, N., Collettini, C., Faulkner, D. R., & Trippetta, F., (2008). Fault zone architecture and deformation processes within evaporitic rocks in the upper crust. *Tectonics*, *27*. https://doi.org/10.1029/2007TC002230

Dieterich, J. H. (1979). Modeling of rock friction 1. Experimental results and constitutive equations. *Journal of Geophysical Research: Solid Earth*, *84*, 2161–2168. https://doi.org/10.1029/JB084iB05p02161

Dieterich, J. H., & Kilgore, B. D. (1994). Direct observation of frictional contacts: New insights for state-dependent properties. *Pure and Applied Geophysics*, *143*, 283–302. https://doi.org/10.1007/BF00874332

Eshelby, J. D. (1959). The elastic field outside an ellipsoidal inclusion. *Proceedings of the Royal Society of London Series A* , *252*, 561–569. https://doi.org/10.1098/rspa.1959.0173

Fagereng, Å., & Beall, A. (2021). Is complex fault zone behavior a reflection of rheological heterogeneity? *Philosophical Transactions of the Royal Society A: Mathematical, Physical and Engineering Sciences*, *379*, 20190421. https://doi.org/10.1098/rsta.2019.0421

Fagereng, Å., Hillary, G. W. B., & Diener, J. F. A. (2014). Brittle-viscous deformation, slow slip, and tremor. *Geophysical Research Letters*, *41*, 4159–4167. https://doi.org/10.1002/2014GL060433

Fagereng, Å., Remitti, F., & Sibson, R. H. (2010). Shear veins observed within anisotropic fabric at high angles to the maximum compressive stress. *Nature Geoscience*, *3*, 482–485. https://doi.org/10.1038/ngeo898

Goebel, T. H. W., Kwiatek, G., Becker, T. W., Brodsky, E. E., & Dresen, G. (2017). What allows seismic events to grow big?: Insights from *b*-value and fault roughness analysis in laboratory stick-slip experiments. *Geology*, *45*, 815–818. https://doi.org/10.1130/G39147.1

Gu, J. C., Rice, J. R., Ruina, A. L., & Tse, S. T. (1984). Slip motion and stability of a single degree of freedom elastic system with rate and state dependent friction. *Journal of the Mechanics and Physics of Solids*, *32*, 167–196. https://doi.org/10.1016/0022-5096(84)90007-3

Han, R., Hirose, T., & Shimamoto, T. (2010). Strong velocity weakening and powder lubrication of simulated carbonate faults at seismic slip rates. *Journal of Geophysical Research: Solid Earth*, *115*, B03412. https://doi.org/10.1029/2008JB006136

Harbord, C. W. A., Nielsen, S. B., De Paola, N., & Holdsworth, R. E. (2017). Earthquake nucleation on rough faults. *Geology*, *45*, 931–934. https://doi.org/10.1130/G39181.1

Hayward, K. S., & Cox, S. F. (2017). Melt welding and its role in fault reactivation and localization of fracture damage in seismically active faults. *Journal of Geophysical Research: Solid Earth*, *122*, 9689–9713. https://doi.org/10.1002/2017JB014903

Hobbs, B., & Ord, A. (2014). *Structural geology: The mechanics of deforming metamorphic rocks, structural geology: The mechanics of deforming metamorphic rocks*. Elsevier. https://doi.org/10.1016/C2012-0-01215-X

Ikari, M. J., & Hüpers, A. (2021). Velocity-weakening friction induced by laboratory-controlled lithification. *Earth and Planetary Science Letters*, *554*, 116682. https://doi.org/10.1016/j.epsl.2020.116682

Ikari, M. J., Marone, C., & Saffer, D. M. (2011). On the relation between fault strength and frictional stability. *Geology*, *39*, 83–86. https://doi.org/10.1130/G31416.1

Ikari, M. J., Niemeijer, A. R., & Marone, C. (2011). The role of fault zone fabric and lithification state on frictional strength, constitutive behavior, and deformation microstructure. *Journal of Geophysical Research: Solid Earth*, *116*, 1–25. https://doi.org/10.1029/2011JB008264

Im, K., Saffer, D., Marone, C., & Avouac, J. P. (2020). Slip-rate-dependent friction as a universal mechanism for slow slip events. *Nature Geoscience*, *13*, 705–710. https://doi.org/10.1038/s41561-020-0627-9

Karner, S. L., & Marone, C. (1998). The effect of shear load on frictional healing in simulated fault gouge. *Geophysical Research Letters*, *25*, 4561–4564. https://doi.org/10.1029/1998GL900182

Kirkpatrick, J. D., Fagereng, Å., & Shelly, D. R. (2021). Geological constraints on the mechanisms of slow earthquakes. *Nature Reviews Earth & Environment*, *24*(2), 285–301. https://doi.org/10.1038/s43017-021-00148-w

Kostrov, B. V. (1974). Crack propagation at variable velocity. *Journal of Applied Mathematics and Mechanics*, *38*, 511–519. https://doi.org/10.1016/0021-8928(74)90047-1

Leeman, J. R., Saffer, D. M., Scuderi, M. M., & Marone, C. (2016). Laboratory observations of slow earthquakes and the spectrum of tectonic fault slip modes. *Nature Communications*, *7*, 1–6. https://doi.org/10.1038/ncomms11104

Liu, Y., & Rice, J. R. (2007). Spontaneous and triggered aseismic deformation transients in a subduction fault model. *Journal of Geophysical Research: Solid Earth*, *112*, 1–23. https://doi.org/10.1029/2007JB004930

Mair, K., Frye, K. M., & Marone, C. (2002). Influence of grain characteristics on the friction of granular shear zones. *Journal of Geophysical Research: Solid Earth*, *107*, ECV41–ECV49. https://doi.org/10.1029/2001jb000516

Mair, K., & Marone, C. (1999). Friction of simulated fault gouge for a wide range of velocities and normal stresses. *Journal of Geophysical Research: Solid Earth*, *104*, 28899–28914. https://doi.org/10.1029/1999JB900279

Marone, C. (1998). Laboratory-derived friction laws and their application to seismic faulting. *Annual Review of Earth and Planetary Sciences*, *26*, 643–696. https://doi.org/10.1146/annurev.earth.26.1.643

Marone, C., & Kilgore, B. (1993). Scaling of the critical slip distance for seismic faulting with shear strain in fault zones. *Nature*, *362*, 618–621. https://doi.org/10.1038/362618a0

Marone, C., & Scholz, C. H. (1989). Particle-size distribution and microstructures within simulated fault gouge. *Journal of Structural Geology*, *11*, 799–814. https://doi.org/10.1016/0191-8141(89)90099-0

McGarr, A., Bekins, B., Burkardt, N., Dewey, J., Earle, P., Ellsworth, W., et al. (2015). Coping with earthquakes induced by fluid injection. *Science*, *347*, 830–831. https://doi.org/10.1126/science.aaa0494

McLaskey, G. C., Kilgore, B. D., Lockner, D. A., & Beeler, N. M. (2014). Laboratory generated M -6 earthquakes. *Pure and Applied Geophysics*, *171*, 2601–2615. https://doi.org/10.1007/s00024-013-0772-9

Mclaskey, G. C., & Yamashita, F. (2017). Slow and fast ruptures on a laboratory fault controlled by loading characteristics. *Journal of Geophysical Research: Solid Earth*, *122*, 3719–3738. https://doi.org/10.1002/2016JB013681

Mena, B., Martin Mai, P., Olsen, K. B., Purvance, M. D., & Brune, J. N. (2010). Hybrid broadband ground-motion simulation using scattering green's functions: Application to large-magnitude events. *Bulletin of the Seismological Society of America*, *100*, 2143–2162. https://doi.org/10.1785/0120080318

Miller, S. A., Collettini, C., Chiaraluce, L., Cocco, M., Barchi, M., & Kaus, B. J. P. (2004). Aftershocks driven by a high-pressure CO_2 source at depth. *Nature*, *427*, 724–727. https://doi.org/10.1038/nature02251

Mitchell, T. M., Toy, V., Di Toro, G., Renner, J., & Sibson, R. H. (2016). Fault welding by pseudotachylyte formation. *Geology*, *44*, 1059–1062. https://doi.org/10.1130/G38373.1

Muhuri, S. K., Dewers, T. A., Scott, T. E. Jr., & Reches, Z. (2003). Interseismic fault strengthening and earthquake-slip instability: Friction or cohesion? *Geology*, *31*, 881–884. https://doi.org/10.1130/G19601.1

Nie, S., & Barbot, S. (2021). Seismogenic and tremorgenic slow slip near the stability transition of frictional sliding. *Earth and Planetary Science Letters*, *569*, 117037. https://doi.org/10.1016/j.epsl.2021.117037

Nielsen, S., Spagnuolo, E., Violay, M., Smith, S., Di Toro, G., & Bistacchi, A. (2016). G: Fracture energy, friction and dissipation in earthquakes. *Journal of Seismology*, *20*, 1187–1205. https://doi.org/10.1007/s10950-016-9560-1

Niemeijer, A., Marone, C., & Elsworth, D. (2010). Frictional strength and strain weakening in simulated fault gouge: Competition between geometrical weakening and chemical strengthening. *Journal of Geophysical Research: Solid Earth*, *115*, 1–16. https://doi.org/10.1029/2009JB000838

Niemeijer, A. R., & Spiers, C. J. (2007). A microphysical model for strong velocity weakening in phyllosilicate-bearing fault gouges. *Journal of Geophysical Research: Solid Earth*, *112*. https://doi.org/10.1029/2007JB005008

Passelègue, F. X., Almakari, M., Dublanchet, P., Barras, F., Fortin, J., & Violay, M. (2020). Initial effective stress controls the nature of earthquakes. *Nature Communications*, *11*, 1–8. https://doi.org/10.1038/s41467-020-18937-0

Passelègue, F. X., Aubry, J., Nicolas, A., Fondriest, M., Deldicque, D., Schubnel, A., & Toro, G. D. (2019). From fault creep to slow and fast earthquakes in carbonates. *Geology*, *47*(8), 744–748.

Passelègue, F. X., Schubnel, A., Nielsen, S., Bhat, H. S., Deldicque, D., & Madariaga, R. (2016). Dynamic rupture processes inferred from laboratory microearthquakes. *Journal of Geophysical Research: Solid Earth*, *121*, 4343–4365. https://doi.org/10.1002/2015JB012694

Peacock, S. M., & Wang, K. (1999). Seismic consequences of warm vs. cool subduction metamorphism: Examples from southwest and northeast Japan. *Science*, *286*, 937–939. https://doi.org/10.1126/science.286.5441.937

Peng, Z., & Gomberg, J. (2010). An integrated perspective of the continuum between earthquakes and slow-slip phenomena. *Nature Geoscience*, *3*, 599–607. https://doi.org/10.1038/ngeo940

Pozzi, G., De Paola, N., Nielsen, S. B., Holdsworth, R. E., Tesei, T., Thieme, M., & Demouchy, S. (2021). Coseismic fault lubrication by viscous deformation. *Nature Geoscience*, *14*, 437–442. https://doi.org/10.1038/s41561-021-00747-8

Renard, F., Beauprêtre, S., Voisin, C., Zigone, D., Candela, T., Dysthe, D. K., & Gratier, J. P. (2012). Strength evolution of a reactive frictional interface is controlled by the dynamics of contacts and chemical effects. *Earth and Planetary Science Letters*, *341*(344), 20–34. https://doi.org/10.1016/j.epsl.2012.04.048

Renard, F., Gratier, J. P., & Jamtveit, B. (2000). Kinetics of crack-sealing, intergranular pressure solution, and compaction around active faults. *Journal of Structural Geology*, *22*, 1395–1407. https://doi.org/10.1016/S0191-8141(00)00064-X

Rowe, C. D., & Griffith, W. A. (2015). Do faults preserve a record of seismic slip: A second opinion. *Journal of Structural Geology*, *78*, 1–26. https://doi.org/10.1016/j.jsg.2015.06.006

Sammis, C. G., & Ben-Zion, Y. (2008). Mechanics of grain size reduction in fault zones. *Journal of Geophysical Research: Solid Earth*, *113*, B02306. https://doi.org/10.1029/2006JB004892

Scuderi, M. M., Collettini, C., Viti, C., Tinti, E., & Marone, C. (2017). Evolution of shear fabric in granular fault gouge from stable sliding to stick-slip and implications for fault slip mode. *Geology*, *45*, 731–734. https://doi.org/10.1130/G39033.1

Scuderi, M. M., Marone, C., Tinti, E., Di Stefano, G., & Collettini, C. (2016). Precursory changes in seismic velocity for the spectrum of earthquake failure modes. *Nature Geoscience*, *9*, 695–700. https://doi.org/10.1038/ngeo2775

Scuderi, M. M., Niemeijer, A. R., Collettini, C., Marone, C., & Big, D. (2013). Frictional properties and slip stability of active faults within carbonate-evaporite sequences: The role of dolomite and anhydrite. *Earth and Planetary Science Letters*, *369–370*, 220–232. https://doi.org/10.1016/j.epsl.2013.03.024

Scuderi, M. M., Tinti, E., Cocco, M., & Collettini, C. (2020). The role of shear fabric in controlling breakdown processes during laboratory slow-slip events. *Journal of Geophysical Research: Solid Earth*, *125*. https://doi.org/10.1029/2020JB020405

Segall, P., Rubin, A. M., Bradley, A. M., & Rice, J. R. (2010). Dilatant strengthening as a mechanism for slow slip events. *Journal of Geophysical Research: Solid Earth*, *115*, 1–37. https://doi.org/10.1029/2010JB007449

Shreedharan, S., Bolton, D. C., Rivière, J., & Marone, C. (2020). Preseismic fault creep and elastic wave amplitude precursors scale with lab earthquake magnitude for the continuum of tectonic failure modes. *Geophysical Research Letters*, *47*, 1–10. https://doi.org/10.1029/2020GL086986

Sibson, R. H. (1977). Fault rocks and fault mechanisms. *Journal of the Geological Society*, *133*, 191–213. https://doi.org/10.1144/gsjgs.133.3.0191

Sibson, R. H. (1992). Implications of fault-valve behavior for rupture nucleation and recurrence. *Tectonophysics*, *211*, 283–293. https://doi.org/10.1016/0040-1951(92)90065-E

Smith, S. A. F., Nielsen, S., & Di Toro, G. (2015). Strain localization and the onset of dynamic weakening in calcite fault gouge. *Earth and Planetary Science Letters*, *413*, 25–36. https://doi.org/10.1016/j.epsl.2014.12.043

Tarling, M. S., Smith, S. A. F., & Scott, J. M. (2019). Fluid overpressure from chemical reactions in serpentinite within the source region of deep episodic tremor. *Nature Geoscience*, *12*, 1034–1042. https://doi.org/10.1038/s41561-019-0470-z

Tarling, M. S., Smith, S. A. F., Viti, C., & Scott, J. M. (2018). Dynamic earthquake rupture preserved in a creeping serpentinite shear zone. *Nature Communications*, *9*, 3552. https://doi.org/10.1038/s41467-018-05965-0

Tenthorey, E., Cox, S. F., & Todd, H. F. (2003). Evolution of strength recovery and permeability during fluid-rock reaction in experimental fault zones. *Earth and Planetary Science Letters*, *206*, 161–172. https://doi.org/10.1016/S0012-821X(02)01082-8

Tinti, E., Fukuyama, E., Piatanesi, A., & Cocco, M. (2005). A kinematic source-time function compatible with earthquake dynamics. *Bulletin of the Seismological Society of America*, *95*, 1211–1223. https://doi.org/10.1785/0120040177

Tinti, E., Scuderi, M. M., Scognamiglio, L., Di Stefano, G., Marone, C., & Collettini, C. (2016). On the evolution of elastic properties during laboratory stick-slip experiments spanning the transition from slow slip to dynamic rupture. *Journal of Geophysical Research: Solid Earth*, *121*, 8569–8594. https://doi.org/10.1002/2016JB013545

van den Ende, M. P. A., Chen, J., Ampuero, J. P., & Niemeijer, A. R. (2018). A comparison between rate-and-state friction and microphysical models, based on numerical simulations of fault slip. *Tectonophysics*, *733*, 273–295. https://doi.org/10.1016/j.tecto.2017.11.040

van den Ende, M. P. A., & Niemeijer, A. R. (2019). An investigation into the role of time-dependent cohesion in interseismic fault restrengthening. *Scientific Reports*, *9*, 1–11. https://doi.org/10.1038/s41598-019-46241-5

Verberne, B. A., Plümper, O., & Spiers, C. J. (2019). Nanocrystalline principal slip zones and their role in controlling crustal fault rheology. *Minerals*, *9*, 328. https://doi.org/10.3390/min9060328

Vidale, J. E., Elisworth, W. L., Cole, A., & Marone, C. (1994). Variations in rupture process with recurrence interval in a repeated small earthquake. *Nature*, *368*, 624–626. https://doi.org/10.1038/368624a0

Yasuhara, H., Marone, C., & Elsworth, D. (2005). Fault zone restrengthening and frictional healing: The role of pressure solution. *Journal of Geophysical Research*, *110*, B06310. https://doi.org/10.1029/2004JB003327

Yoffe, E. H. (1951). The moving griffith crack. *Philosophical Magazine*, *42*, 739–750. https://doi.org/10.1080/14786445108561302